

Absolute total and partial dissociative cross sections of pyrimidine at electron and proton intermediate impact velocities

Wania Wolff,^{1,a)} Hugo Luna,¹ Lucas Sigaud,¹ Andre C. Tavares,²
and Eduardo C. Montenegro¹

¹*Instituto de Física, Universidade Federal do Rio de Janeiro, PO 68528, 21941-972 Rio de Janeiro, RJ, Brazil*

²*Departamento de Física, Pontifícia Universidade Católica do Rio de Janeiro, PO 38071, Rua Marquês de São Vicente 225, 22453-900 Rio de Janeiro, RJ, Brazil*

(Received 11 October 2013; accepted 24 January 2014; published online 12 February 2014)

Absolute total non-dissociative and partial dissociative cross sections of pyrimidine were measured for electron impact energies ranging from 70 to 400 eV and for proton impact energies from 125 up to 2500 keV. MOs ionization induced by coulomb interaction were studied by measuring both ionization and partial dissociative cross sections through time of flight mass spectrometry and by obtaining the branching ratios for fragment formation via a model calculation based on the Born approximation. The partial yields and the absolute cross sections measured as a function of the energy combined with the model calculation proved to be a useful tool to determine the vacancy population of the valence MOs from which several sets of fragment ions are produced. It was also a key point to distinguish the dissociation regimes induced by both particles. A comparison with previous experimental results is also presented. © 2014 AIP Publishing LLC. [<http://dx.doi.org/10.1063/1.4864322>]

I. INTRODUCTION

Electron, photon, and heavy ions interactions with biologically important molecules have been a subject of study for many years, but recently more attention has been dedicated to some key species such as purine and pyrimidine and their derivatives, the nucleic acids bases. Deeper knowledge of the processes that take place in the biological media is desirable for many biomedical and astrochemical applications, which need accurate models that include a comprehensive amount of data related to the interaction of these ionizing agents (electron, photon, and heavy ion) from sub-ionization thresholds to high energies. Electrons and protons transfer their kinetic energies to the biological tissue through processes such as molecular excitation or ionization which can be followed by molecular dissociation.¹ These dissociated molecules produced inside the exposed cells or in their surroundings affect the cellular responses, causing malfunctioning or mutations and affecting the likelihood of the cells survival. This is a very complex chain of physical, physical-chemical, and biological processes, whose studies and applications in areas as diverse as ion beam cancer therapy, diagnostic tests, radio-dosimetry, radiation protection in space and terrestrial environments, and proton irradiation effects of solar particles and cosmic rays on space exploration rely on basic input data provided by biomolecular ionization experiments.¹ Indeed, for a deeper understanding of the effects of ionizing radiation on the microscopic level, the quantification of excitation, ionization and fragmentation as well as the energy transfer and energy deposition induced by a variety of heavy ions and electrons is needed.

Pyrimidine (C₄H₄N₂) is a heterocyclic aromatic organic compound similar to benzene, C₆H₆, containing four carbon atoms and two nitrogen atoms at positions 1 and 3 of the six-membered ring (Fig. 1(a)). The molecule is the building block of three of the five DNA/RNA bases: cytosine, thymine, and uracil.² The approach of using smaller molecules with structural similarities in the gas phase and then comparing them with their larger derivatives in biological systems is an useful and widely used methodology to investigate the effects of ionizing agents on complex bio-molecules.

Besides the bio-chemical relevance of the pyrimidines, they are also important for astro-chemistry,^{3–6} since they have also been detected on meteorites, as a result of interstellar chemistry. The investigation of the fragmentation pattern and the resistance of the molecules to ionizing agents can elucidate the origin of these molecules in the interstellar medium as well as how they survive in space.^{7,8}

The limited ionization data available for charged particles impinging on pyrimidine come mainly from electron impact measurements. Mass spectra of compounds containing the pyrimidine ring were first obtained by Biemann and McCloskey,⁹ followed by the work of Rice *et al.*,^{2,10} where the mass spectra of the pyrimidine itself and a series of chemically modified pyrimidines were measured. These works were followed by studies of deuterium substituted pyrimidine carried out by Milani-Nejad and Stidham.¹¹ From the spectra of the deuterated species, they concluded that the splitting of HCN from the pyrimidine ring is produced by the loss of the 4 position carbon. More recently, Linert *et al.*¹² measured total and partial ionization cross sections with electron impact energies ranging from near ionization thresholds (9 – 10 eV) up to 150 eV. From the yield curves in the near threshold region, they extracted the appearance energies of several fragments (18 fragments) and compared them with

^{a)}Electronic mail: wania@if.ufrj.br

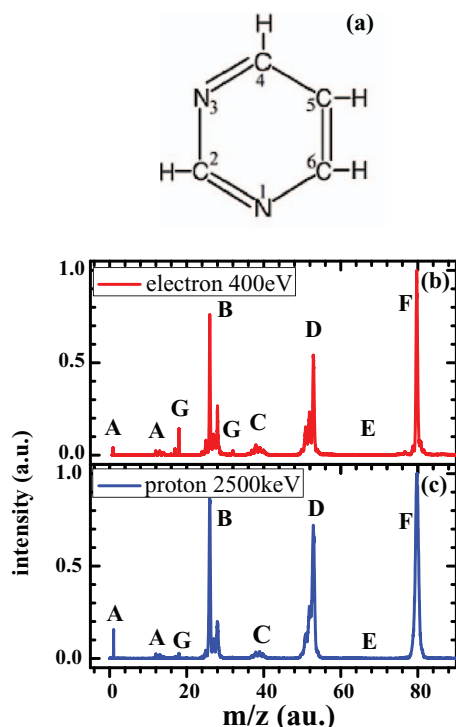


FIG. 1. (a) Schematic molecular structure of pyrimidine; time of flight spectra of pyrimidine at (b) 400 eV electrons; and (c) 2500 keV protons. The labels A, B, C, D, E, F, and G included at the top each fragments group designate fragmentation pathways and the contamination peaks (see text).

electron impact and photoionization measurements of Momigny *et al.*¹³ and Schwell *et al.*,¹⁴ respectively. Electron momentum distributions of the outer valence orbitals at electron energies of 600 and 1500 eV were reported by Ning *et al.*¹⁵ and triple differential cross section for ionization was measured at incident energy of 250 eV by Builth *et al.*¹⁶ The dissociative excitation into excited atomic fragments was addressed by Hein *et al.*¹⁷ measuring the emission cross section in the VUV spectral region from ionization threshold to 375 eV. In special, the possible channels and their contribution leading to the production of excited H(2p) were discussed. Besides the very low energy (10 to 22 eV) studies of rate coefficients for several ions performed by Fondren *et al.*,¹⁸ measurements of ionization and fragmentation of pyrimidine by heavy ion impact is essentially nonexistent. Mendoza *et al.*¹⁹ presented recently a photo-desorption study from frozen pyrimidine around the N 1s edge focused on astrochemistry and included preliminary data on the destruction of pyrimidine in gas phase caused by proton at an energy of 2500 keV. (The present branching ratios at proton energy of 2500 keV differ from those of Ref. 19, where the contribution of the parent molecule ion was underestimated due to error in data processing.)

In this work, we have measured absolute electron and proton cross sections for ionization of pyrimidine, including the parent ion as well as 24 fragment products. The electron energy ranges from 70 to 400 eV and extends the previous measurements¹² to velocities high enough to ensure the equivalence of the single ionization cross sections for equivalent

electron and proton impact, as supported by first order theories.²⁰

Protons cross sections for the same fragment ions measured for electron impact were obtained from 125 up to 2500 keV. These measurements verify if the assumption of the equivalence of the fragmentation pattern produced by these two projectiles indeed breaks down, as found many years ago by Wexler²⁰ for other molecular species.

The collision time at our highest measured proton energy is within a fraction of an attosecond. In this case, the pattern produced in the fragmentation corresponds to post-collisional de-excitation of the molecule, giving rise to a spectroscopic signature of the molecular orbital in which the primary vacancy is produced. Taking advantage of the reliability of some semi-empirical models to describe primary vacancy production by electrons and protons,^{21,22} it was possible to obtain the branching ratios associated to the various molecular orbitals which result in the measured fragmentation fractions of pyrimidine.

The paper is organized as follows. In Sec. II, the experimental procedures used in this work are described. The results and discussions are presented in Sec. III, while in Sec. IV a scheme is proposed to obtain the contribution from the various valence Molecular Orbitals (MO) to the fragment ions yield. Finally, in Sec. V, the main conclusions are drawn.

II. EXPERIMENTAL PROCEDURE

The current experiments were carried out at the Federal University of Rio de Janeiro. The experimental set-ups and the procedures adopted for the determination of the absolute cross sections for electron and proton impact were described in detail in Refs. 21 and 23, respectively, and a brief description of both set-ups are presented here.

A. Ion beam set-up

A proton beam with energies ranging from 125 to 2500 keV was obtained from a Pelletron accelerator. The ion beam was mass-charge selected and directed by a dipole switch magnet towards the collision chamber, where it crosses a target gas jet at a right angle. The beam profile was defined to an area less than 2 mm² and its positions with respect to the center of the extracting electrodes of the Time-of-Flight (TOF) spectrometer and to the effusive pyrimidine gas jet were fine adjusted. The base pressure in the transport line and in the collision chamber was about $2 - 3 \times 10^{-8}$ Torr. With the pyrimidine gas jet, the working background pressure in the collision chamber was typically of 10^{-6} Torr.²³

After the interaction of the proton beam with the gaseous target, the ejected electrons and ionic fragments were extracted from the interaction region by means of a static electric field (700 V/cm), focused and accelerated into a field-free drift tube, and directed to the detectors. The ions were collected by a micro-channel plate detector (MCP) in chevron configuration, and the electrons by a channeltron, placed in the opposite direction. Both detector signals after amplification and CFD discrimination were sent to a fast time to digital converter (TDC) and the start-stop signals recorded.

The mass resolution of the spectrometer was optimized by measuring time of flight spectra of Kr with its 6 stable isotopes ($m = 78 - 86$) and the variation of the peak widths of single ionized noble gases was investigated. As previously described,²⁴ the mass efficiency of the ion detector was obtained by measuring single and multiple ionization of Ne, Ar, Kr, and Xe. It resulted that the TOF analyzer did not show any significant transmission dependence with the recoil ion mass.

B. Electron set-up

The electrons were produced in the 70 – 400 eV energy range by an electron gun operating in a pulse mode configuration. The electron gun delivers 1 – 2 pA, measured by a Faraday Cup positioned at the end of the gas cell. The stream of electrons was defined by pulses of 50 ns width and 20 MHz repetition rate. The beam was guided through a pressure controlled gas cell which was filled with the sublimated pyrimidine. The working pressure inside the cell was kept below 5×10^{-4} Torr, thus ensuring measurements in the single collision regime, and monitored continuously by a capacitance manometer, therefore allowing the measurement of the absolute target density. The interaction region of 28 mm^2 was defined by a collimator at the entrance of the TOF drift tube.²¹

A pulse extraction of 50 kV/m and time-width of $10 \mu\text{s}$ was applied across the interaction region in synchronism with the trailing edge of the electron beam pulses in order to collect any positively charged ions and fragments produced by the ionizing events. After extracted, the ions were guided through a TOF drift tube, and were detected by a MCP. The extraction pulses were used to trigger the experiment and provided the start signal of the TDC. The output signal of the fragment ion detector (MCP) delivered the stop signal to the TDC. A capacitive load, given to the pulsing electronics by the extraction field at the interaction region, resulted in a minimum delay of 500 ns between the electron beam and the extraction electrical field pulses, which can account for the loss of some of the faster, more energetic fragments, like H^+ .²⁵ The collection efficiency of the MCP detector was calibrated with an efficiency curve obtained by measuring H_2 , He, Ne, N_2 , Ar, and Kr ionization cross sections and following the correction procedure of Takashashi *et al.*²⁶ Therefore, since the number of incident particles, the number of scattering centers and the detector efficiency were directly measured, absolute ionization and dissociative cross sections were obtained using this experimental set-up.

C. Uncertainties

In the electron case, the uncertainties of the partial yields associated with ion counts were negligible, less than 1%, since the measurements were taken with peak areas ranging $10^3 - 10^5$ counts and the peaks were well discriminated. The uncertainty of the absolute cross sections is associated with the counts of the peak, combined with the uncertainties of the absolute pressure of the sublimated sample, electron current, and efficiency correction of the ion collection. The un-

certainty was minimized by measuring the pressure and the electron current with fluctuations of less than 1%. The cross section uncertainty associated to MCP efficiency is of the order of 2%. The overall uncertainties are below 6%. The loss of the energetic H^+ ions did not affect the total cross sections because its value is an order of magnitude smaller than of each of the absolute cross sections of the most intense fragments.

In the proton case, for some masses, it was required to adopt a fitting procedure (multiple Gaussian line shapes) to obtain the areas under the peaks, whose ion counts ranged from 3×10^2 to 5×10^4 counts. The accuracy of the fitted peak areas, evaluated by two data analysis programs, resulted in uncertainties in the branching ratios that, in the average, were 8%. The uncertainty of the non-dissociative cross section for electron impact was evaluated less than 5% and therefore the uncertainty of the absolute cross sections for fragment production was estimated below 10% and marginally higher for fragments ions with low cross section values.

D. Sample preparation and injection

Collision experiments with complex bio-molecules in the gas phase are challenging due to the difficulties in the preparation of well-characterized gas targets and in the accurate determination of its absolute number density. The samples must be pure, free of contaminants, and not degraded during the heating and sublimation process.²⁷⁻²⁹ Because of these difficulties, some studies with pyrimidines derivatives opted to normalize their experimental results to a calculation at a fixed energy.^{30,31}

All samples used in this work were purchased from Sigma-Aldrich and Alpha Aesar with purity higher than 99% and used without further purification. At room temperature, pyrimidine is liquid, very hygroscopic, and photosensitive. Therefore, special care was taken when inserting the pyrimidine sample in the target injection line outside the vacuum chamber. The sample ampoule was opened under Argon atmosphere and pipetted into the glass culture tubes filled with some micro-porous molecular sieves. The sample setup sealed under Argon was then attached to the gas injection line. Before opening the sample to the collision chamber the liquid sample was frozen with water-ice and the system pumped off the absorbed gas. At room temperature, the vapor pressure of the sample was high enough to achieve a gas density in the interaction region which allows the mass spectra to be recorded, without needing to further heat the sample.

The gaseous pyrimidine has its flow from a reservoir controlled by a leak valve and it is introduced into the interaction region through a needle, in the proton set up case, or through a gas line filling a gas cell large enough so that the target gas is in thermal equilibrium, in the electron set-up. The gas flow rate was maintained free of fluctuation during hours by using a water-ice bath, held at a temperature close to freezing the sample. This procedure has the advantage of eliminating almost all water or other contamination at the interaction region and of avoiding possible thermal modifications with or without isomerization of the pyrimidine.

III. RESULTS AND DISCUSSION

A. Fragment ion spectra

In Figures 1(b) and 1(c), spectra for the highest impact energies measured, that is, for 400 eV electrons ($v = 5.4$ a.u.) and for 2500 keV protons ($v = 10$ a.u.), respectively, are presented.

These spectra are normalized to the peak maximum of the parent molecule, showing that the same groups of peaks appear in both spectra. This similarity indicates that the main fragmentation pathways do not depend on the type of the projectile, at least for swift projectiles. The group composition of the spectra is typical for DNA/RNA bases and pyrimidines and purines derivatives under interaction with charged particles.^{2,10,30–36} The spectra are well structured, with clearly defined groups of peaks. Each group, labeled on the top of the peaks-group by A, B, C, D, E, and F, corresponds to fragments with specific number of atoms of the original aromatic ring, or equivalently, to the loss of one and more carbon or nitrogen atoms. It is noteworthy that group E, which would have fragments containing 5 atoms of the ring, is totally absent, as already noticed in previous studies on electron induced pyrimidine fragmentation.^{2,11,12} The group G is associated to small amounts of contamination present in the system, mostly water and air molecules.

The dominant peak in the spectra corresponds to the pyrimidine parent ion ($C_4H_4N_2^+$). The other major fragment ions have $m/z = 26$ and 53, and have approximately the same intensity. A total of 25 different ionic fragments were observed and listed in Table I, divided in 5 distinct groups, namely, A, B, C, D, and F, with all possible major and minor fragment ions identified.

These fragments arise from the fragmentation of the excited parent molecule (p^+) into two or three moieties, with stable or excited charged molecular ions, and the complementary loss of neutral molecules and atoms, and sometimes migration of H atoms. The formation of the charged fragments are discussed in detail in Rice *et al.*,² Linert *et al.*,¹² Schwell *et al.*,¹⁴ Vall-Iloera *et al.*,³⁷ Lin *et al.*,³⁸ and references therein. The mass-ion species assignments assumed later on in this work are indicated by bold letters in Table I. The main ion species were selected based on experimental and theoretical studies presented in these references. However, the other ionic assignments cannot be ruled out, but they may be considered unlikely. As previously noted, the ejection

of the HCN molecule (thermodynamic stable) dominates the fragmentation process.

The formation of stable doubly charged pyrimidine could not be totally ruled out, but appearance of the peak corresponding to $m/z = 40$ is likely associated to the $C_2H_2N^+$ fragment. Pyrimidine derivatives, as uracil, thymine and cytosine, do not show any indication of stable doubly charged states in the mass spectrum associated to ionization by charged particles,^{30–36} whereas the purine derivative, adenine, shows an indication of a surviving double charged parent ion, when neutral and singly charged keV particles are used as projectiles.³³

The contribution of residual air is only slightly present in the electron spectra (O_2^+) while both spectra depict some water contamination. If the “sample filling procedure” described in the experimental section is not used, a huge water contamination is observed. In the proton data no contribution of N_2^+ and CO^+ to the peak at $m/z = 28$ is observed, while in the electron case a small contribution is present. The ionization of N_2 from air results in the formation of N_2^+ and N^+ . N_2^+ molecular ion is indistinguishable from $HCNH^+$ and $C_2H_4^+$ as both have $m/z = 28$, and N^+ from the pyrimidine break up. These contributions were subtracted considering the intensity of the O_2^+ peak, distinguishable from the sample fragments as no pyrimidine fragment results with $m/z = 32$, and using cross section data available in the literature.³⁹

The distribution yields of the fragment ions following dissociative ionization are discussed next and presented relative to the parent molecular ion (partial yield) or to the sum of all fragment ions (branching ratio) as function of the projectiles energy or velocity. Afterwards, the absolute non-dissociative and dissociative ionization cross sections are presented for electron impact, followed by the same scheme for proton impact.

B. Electron impact

In Figure 2 fragment ions curves (partial yields) are presented with respect to the parent molecule $C_4H_4N_2^+$ as a function of the electron impact energy. Figures 2(a), 2(b), 2(c), 2(d), and 2(e) display the relative fragment yields for the 5 fragment-groups A, B, C, D, and F, respectively.

Group F is the most intense one and includes the parent ion ($m/z = 80$), the isotopic ($m/z = 81$) ion, and the weak

TABLE I. Molecular mass (m/z) in a.u. and respective ionic fragment species presented divided into the groups A, B, C, D, and F following ionization of pyrimidine. The ionic species indicated in boldface will be used in the text as the fragment species related to that molecular mass.

m/z	Ionic fragment	m/z	Ionic fragment	m/z	Ionic fragment	m/z	Ionic fragment	m/z	Ionic fragment
Group A		Group B		Group C		Group D		Group F	
1	H⁺	24	C₂⁺	36	C₃⁺	50	C₃N⁺	79	C₄H₃N₂⁺
12	C⁺	25	C₂H⁺	37	C₃H⁺	51	C₃HN⁺, C₄H₃⁺	80	C₄H₄N₂⁺
13	CH⁺	26	C₂H₂⁺, CN⁺	38	C₃H₂⁺	52	C₃H₂N⁺, C₄H₄⁺, C₂N₂⁺,	81	¹³C¹²C₃H₄¹⁴N₂⁺, ¹²C₄H₄¹⁵N¹⁴N⁺
14	N⁺	27	HCN⁺, C₂H₃⁺	39	C₃H₃⁺, C₂HN⁺	53	C₃H₃N⁺, C₂HN₂⁺		
15	NH⁺	28	HCNH⁺, C₂H₄⁺	40	C₂H₂N⁺, CN₂⁺	54	¹³C¹²C₂H₃N⁺, C₂H₂N₂⁺, C₃H₄N⁺		
		29	CH₃N⁺	41	CHN₂⁺, C₂H₃N⁺,				

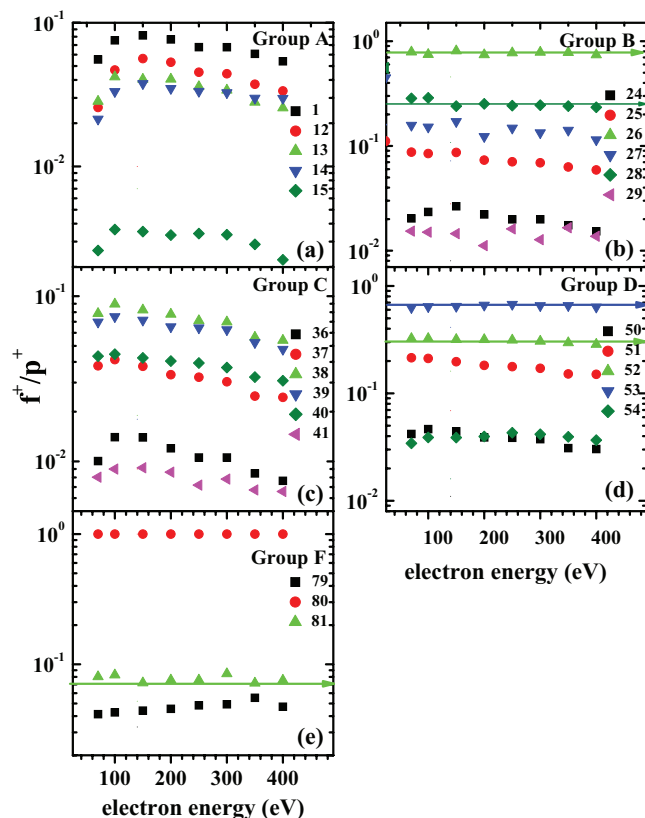


FIG. 2. Partial yields relative to the parent molecule (p^+) for forming fragments ions (f^+) following dissociative ionization as function of the electron energy. (a) Group A, (b) Group B, (c) Group C, (d) Group D, (e) and Group F. The partial yields of the corresponding m/z fragment are indicated by closed symbols. In (b), (c), and (d), horizontal arrows are included in order to guide the eye.

de-hydrogenated ($p - H$) $^+$ ion created by loss of one H atom from the parent cation.^{17,40} One atom removal with and without excitation is an unimportant process consistent with ion dissociative cross section values. The maximum of emission cross section for the $H(2p - 1s)$ transition is around 130 eV electron-impact energy¹⁷ and is ~ 3.5 times lower than the cross section for the ($m/z = 79$) ion presented in this work. There is virtually no $m/z = 78$ ion present in the spectra corresponding to the double H loss channel, although a relative yield of 5% was measured at low VUV photon energies.³⁷ Figure 2(e) displays the low partial yields of the $m/z = 79$ fragment, showing a constant value as function of the impact energy, and of the $m/z = 81$ ion, which value indicates the presence of both ^{13}C and ^{15}N -isotopes in the ring.

Group D is a strong group associated to the rupture of the two weak C – N bonds, in which the fragment ion with $m/z = 53$ presents the third highest yield, as shown in Figure 2(d). All fragments in the $m/z = 50 - 54$ region follow a neutral HCN loss from the parent cation—the stable one as well as the subsequent ions formed by decays with successive losses of H atoms showing a constant yield as function of the energy (see Figure 2(d)). This behavior indicates that the loss of a neutral HCN is likely to be induced by single ionization. It should be mentioned that the photon-ion curves of Ref. 14 show for the masses $m/z = 52 - 53$ a step structure, which could suggest a different path or a different orbital ionization

for these species formation. We note that the $m/z = 54$ ion is identified to isotope C and N atoms present in the cation, as its relative intensity with respect to that of the $m/z = 53$ ion are consistent within the natural abundances of C and N isotopes and appearance energies thresholds.¹²

Group B is also a strong group, associated to the masses $m/z = 24 - 29$, and corresponds to ions of the ring with two C atoms or one C and one N atom. The major fragment of this group, with $m/z = 26$, is considered as coming from the loss of two neutral HCN in sequence,¹⁴ and exhibits the second highest yield, as shown in Figure 2(b). The adjacent lower masses of $m/z = 24 - 25$ are likely formed due to further losses of H atoms. On the other hand, as displayed in Figure 2(b), it is also possible that a charged HCN^+ instead of a neutral one with $m/z = 27$ is formed in the fragmentation process. The charged HCN may also contribute to the formation of the $m/z = 28 - 29$ ions by migration of H atoms to the N atom position, leaving complementary neutral fragment(s) behind. The ions with $m/z = 28$ and 52 have similar yields, as previously noted in electron-ion mass spectrometry¹² and photo-ion mass spectrometry³⁷ studies at 23 eV. The $m/z = 24 - 29$ yields show almost a constant value in the measured energy range. This behavior may indicate that group B fragments can originate from the group D following a single ionization by the projectile electron.

The fragments of group A correspond to the single atomic ions H, C, and N, and to CH^+ and NH^+ , and are originated by multiple break-ups, with the ring splitting into several pieces. Their ratios with respect to the parent ion clearly show a different dependence with the projectile energy as compared with the previously discussed groups B and D: with the increase of the projectile energy, the values initially increase, reach a maximum, and then slowly decrease (see Figure 2(a)).

The fragments of group C are associated to the masses $m/z = 36 - 41$, and correspond to ions of the ring with three C atoms, or two C atoms and a single N atom. The $m/z = 36 - 41$ yields can be related to fragmentation into 2 moieties, one of them neutral, or to sequential ruptures of excited intermediate fragments, losing neutral molecules and atoms. On the other hand, the impact energy dependence of Groups A and C yields, as shown in Fig. 2(c), may indicate that multiple fragmentation following a double-vacancy production by the projectile through a second order, two-step mechanism, may also contribute to the formation of these groups. Indeed, cross sections for two-step vacancy production decrease faster with the increase of the projectile velocity in comparison with the single-step ionization and, therefore, the ratio between two-step and single-step processes decreases with the increase of the projectile energy, accordingly.

The only quantitative relative yields available in the literature for electron impact are from Ref. 12 which reported measurements for electron energies up to 150 eV. These results at an electron energy of 140 eV show systematically lower relative abundances when compared with the present data. Relative yield discrepancies have also been observed between photoionization experiments on amino acids and DNA bases, where Quadrupole Mass Spectrometry^{41,42} or Time of Flight Mass Spectrometry⁴³⁻⁴⁵ were applied. The

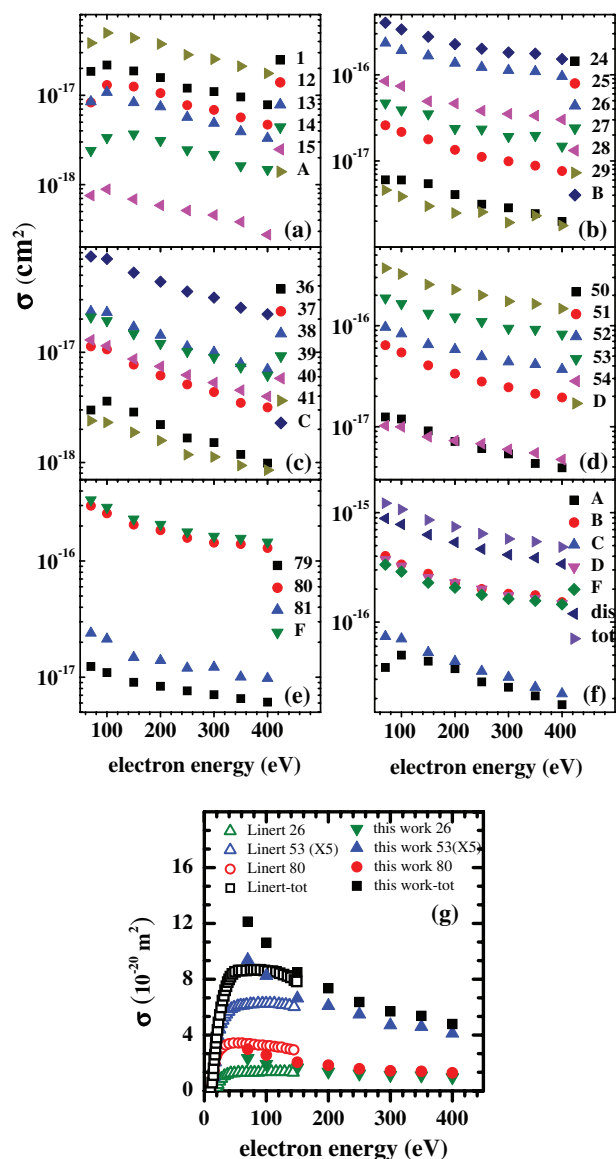


FIG. 3. Absolute non-dissociative and partial dissociative cross sections for electron impact in cm^2 at electron impact energies from 70 eV up to 400 eV. (a) Group A, (b) Group B, (c) Group C, (d) Group D, and (e) Group F. Indicated by closed symbols are the corresponding m/z fragments and the sum labeled by the group letter (A, B, C, D, or F). (f) Sum of the fragments cross section of each group compared together. (g) In linear scale values for $m/z = 26$ and 53 fragmentation cross sections, $m/z = 80$ non-dissociative ionization and total cross section; closed symbols: this work; open symbols: Ref. 12 (both Ref. 12 and present results for $m/z = 53$ were multiplied by 5).

discrepancies can be explained by the different transmission efficiencies of low and high masses, ion optics parameters and ion residence times in the mass spectrometers, as pointed out by Jochims *et al.*⁴²

The non-dissociative and partial dissociative cross sections as function of the electron impact energy are shown in Figure 3 in log scale, separated into Figs. 3(a), 3(b), 3(c), 3(d), and 3(e) which are associated to the 5 fragment-groups, A, B, C, D, and F, respectively. The sums of the cross sections for each peak group are also included in each plot, and Figure 3(f) gives an overall view of the relative contributions of all groups.

In the low energy side, the cross section maxima of groups A and C are clearly present. On the other hand, this is not the case for groups B, D, and F for which the cross section maxima was not yet reached for our lowest measured energy. Indeed, these last groups have the cross sections maxima at lower energies, as indicated by the measurements of Linert *et al.*¹² This behavior is an indication that groups A and C are formed either by a vacancy in a deeper molecular orbital or through a two-step ionization process, thus associated to a higher appearance energy compared to those associated to outer valence ionization. In the measured energy range, fragmentation always supersedes non-dissociative ionization. The values of the fragment cross sections values are given in Table III in the Appendix. A comparison between our results with the measurements of Ref. 12 for $m/z = 26$, $m/z = 53$ (Ref. 12 and present results were multiplied by 5), $m/z = 80$ and the total ionization cross section are depicted in linear scale in Figure 3(g).

C. Proton impact

In Figure 4, we present branching ratios for fragment ions induced by proton impact.

The branching ratio is defined as the relative abundance of each of the molecular ions, f_i^+ , with respect to the sum of all fragments, $\sum_i (f_i^+)$, including the ionized molecule. Figures 4(a), 4(b), 4(c), and 4(d) display the branching ratios of the 5 fragment groups, labeled A, B, C, D, and F. Almost all the ionic fragment ratios of groups A and C show the same dependence with the energy: the ratio is a decreasing function of the collision energy, with a slope, which is more pronounced at lower measured energies. On the other hand, at high energies, the ratios of all the fragment groups are essentially

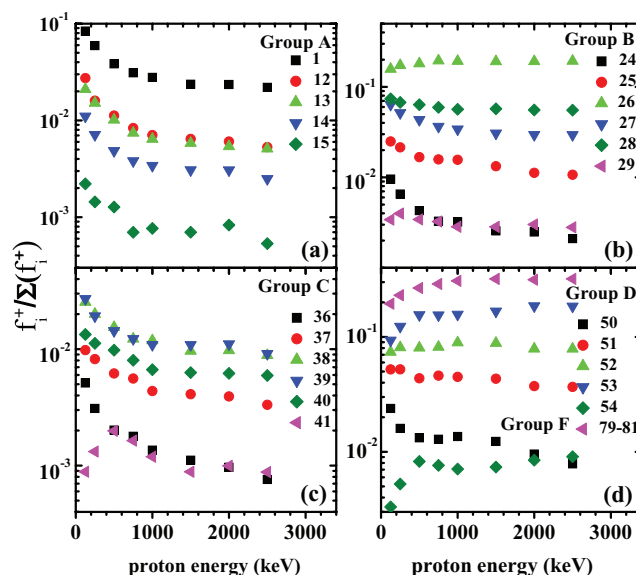


FIG. 4. Branching ratios (f_i) relative to the sum of all fragment ions $\sum_i (f_i^+)$ following non-dissociative and dissociative ionization as function of the proton energy. (a) Group A, (b) Group B, (c) Group C, (d) Group D, and Group F. Indicated by closed symbols are the corresponding m/z fragments.

constant. For the masses $m/z = 41$ and 54 (and somehow $m/z = 29$), the ratios show an increase at the lower impact energies, which may indicate that H-migration (one possible rearrangement channel) tends to be inhibited at these lower collision energies.

The proton experimental setup did not allow direct measurements of the target density, neither of the absolute collection efficiency. Hence the absolute cross sections for collisions with proton beam were obtained through a normalization procedure: the ratio of the sum of fragments with $m/z = 79 - 81$ (SUMF) with respect to the total ions production, $N^{\text{SUMF}}/N^{\text{TOTAL}}$, for both projectiles were compared and it has been verified that their values as a function of the projectile velocity are identical, within the experimental uncertainties. Assuming the mass-independence of the non-dissociative cross sections, as given by the Born approximation¹⁷ in the intermediate-to-high velocity regime used in this work, an allometric function was adjusted to the experimental electron impact cross section (σ_e^{SUMF}) to give $\sigma_p^{\text{SUMF}} = \sigma_e^{\text{SUMF}}$. The total ionization cross sections σ_p^{TOTAL} were finally obtained dividing σ_e^{SUMF} by the corresponding branching ratio f^{SUMF} measured for proton impact.

The dissociative cross sections as a function of the proton energy are displayed in Figure 5, separated into Figs. 5(a), 5(b), 5(c), and 5(d) related to the 4 fragment groups, labeled A, B, C, and D. The sums of the peaks-group cross sections

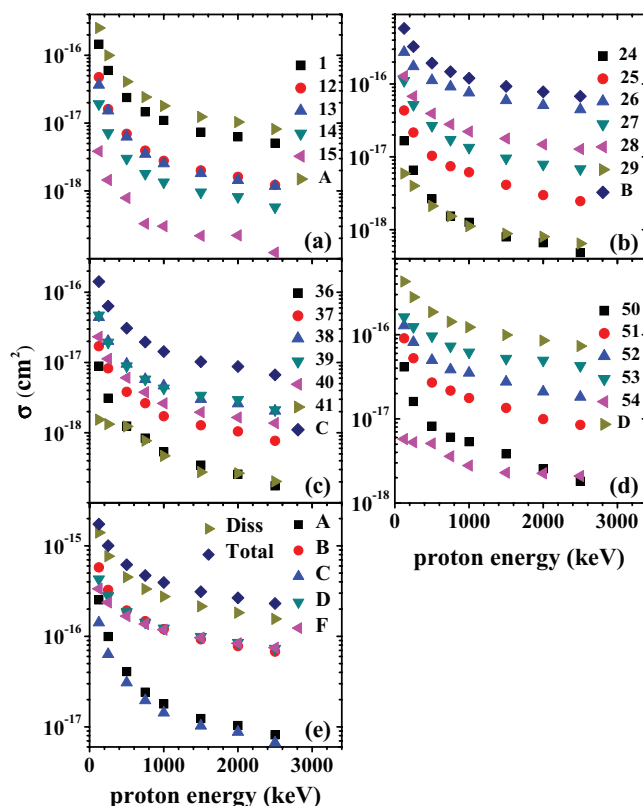


FIG. 5. Absolute non-dissociative and partial dissociative cross sections in cm^2 at proton collision energies from 125 keV up to 2500 keV. (a) Group A, (b) Group B, (c) Group C, and (d) Group D. (e) Sum of the fragments cross section of each group compared together. Indicated by closed symbols are the corresponding m/z fragments and the sum labeled by the group letter (A, B, C, D, or F).

are also included in each of these figures. In order to visualize the contribution from each group to the total cross section, the cross sections for the various groups are presented together in Figure 5(e).

The cross sections of all groups rise with the decrease of the proton energy with the groups A and C rising steeper than the others, a behavior which is associated to a larger degree of fragmentation. On the other hand, group F rises more softly compared to the others, which is due to that the parent ion is the dominant ionic species of this group (see Figure 5(e)). The fragmentation supersedes the ionization in the entire energy range. All fragment cross section values are given in Table IV in the Appendix.

D. Comparison between electron and proton impact as function of the velocity

As in the proton case we are not able to discriminate the peaks with $m/z = 79 - 81$ accurately (Group F), the comparison with electrons was carried out with respect to the peak sum of these three fragments (Sum F). For electrons, these three masses can be discriminated and one can observe that the contribution of the de-hydrogenated fragment $m/z = 79$ is of the order of 3%, while the contribution of the $m/z = 81$, associated with one carbon isotope atom ^{13}C or ^{15}N , is of the order of 6%, meaning that the comparison of the partial yields of the cations, applying the Sum F normalization, does not differ substantially from those of the parent ion.

By comparing all yields of groups A, B, C, and D fragments, shown in Figure 6, the following features become clear: (i) from $3.5v_0$ onwards, all ionic yields extracted from electron and proton impact data are very similar in the overlapping region, except for the atomic H^+ and N^+ yields.

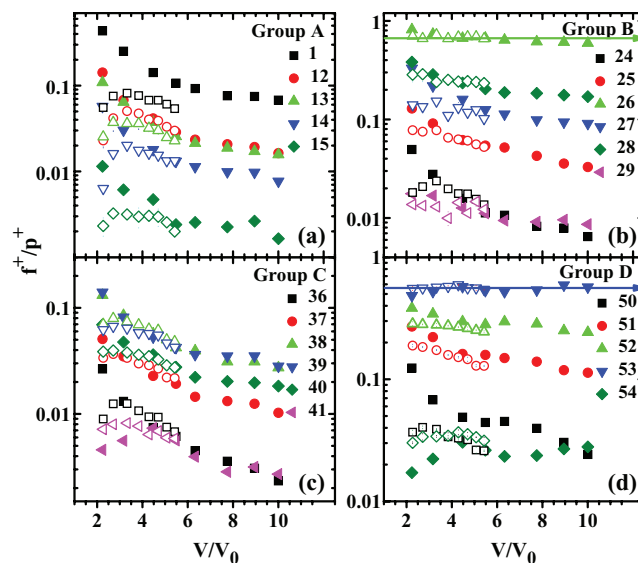


FIG. 6. Comparison of the partial yield relative to the sum of all non-dissociative and de-hydrogenated fragments (Sum F) as function of the projectile velocity expressed in Bohr velocity, v_0 , ranging from $2-10 v_0$. The fragments following ionization are divided into 5 groups: (a) Group A, (b) Group B, (c) Group C, (d) Group D, and (e) Group F. Indicated by symbols are the corresponding m/z fragments. Closed symbols: proton data; open symbols: electron data.

These differences can be explained by the lower collection efficiency of energetic H^+ ions in the electron set-up and by the uncertainties in the subtraction factors applied to take into account the N^+ ion coming from the dissociation of N_2^+ . That may have been overestimated because O_2 and N_2 have different sticking properties in the cell walls. Also, it is noteworthy that the molecular fragment like $m/z = 50$ presents a marked difference between electron and proton impact (see Sec. III E); (ii) from $5.5 v_0$ to $10 v_0$, the proton data show a regular trend, following a slowly decaying curve, with the slope significantly more pronounced for the fragments of the group A and C; (iii) from the lowest to highest velocity used in this work, only the fragments originated from the HCN and $2HCN$ losses ($m/z = 53$ and 26) show an almost constant value for both projectiles as indicated by a horizontal arrow; (iv) from below $3.5 v_0$ to the onset of the measurements, for proton impact the ion yields associated to the groups A and C rise, while for electron impact they decrease. The reason for this difference lies in the fact that in the electron case, as the impact velocity decreases below the maximum, the energy transferred to some deeper MO of the molecule decreases sharply and leads to less effective fragmentation while in the proton case the opposite occurs, as the cross sections maxima are barely reached in the present experiment and more energy is available to be transferred.

E. Total ionization cross sections

Figure 7 shows the absolute ionization cross section from $2 v_0$ to the highest velocity measured for electron and proton impact. The agreement of the electron total ionization cross sections with the results available in the literature¹² over the overlapping velocity region is only fair, since the previous

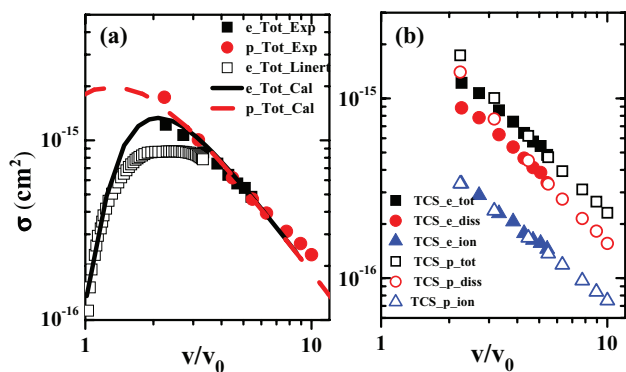


FIG. 7. (a) Experimental total ionization cross section (TCS) for electron and proton impact as function of the projectile velocity expressed in Bohr velocity (v_0); closed square: experimental TCS for electron impact, this work; closed circle: experimental TCS for proton collision, this work; open square: TCS for electron impact of Ref. 12; full line: calculated TCS for electron impact, this work; dash line: calculated TCS for proton collision, this work; (The calculated TCS are summed cross section for the molecular orbitals listed in Table II, while the measured ones are summed cross section for all measured fragment ions.) (b) Closed triangle: Total non-dissociative cross section for electron impact; open triangle: Total non-dissociative cross section for proton collision; closed circle: Total dissociative cross section for electron impact; open circle: Total dissociative cross section for proton collision; closed square: Total cross section for electron impact; open square: Total cross section for proton collision.

data present a flat maximum, in contrast to the present measurements, where such tendency is not seen. The absence of a flat maximum is a marked signature of the electron impact ionization of atoms and small molecules,⁴⁶ as well as of complex biomolecules, such as the DNA components,⁴⁷ although a flat behavior has been reported for the total ionization of thymine⁴⁸ and pyridine.⁴⁹

Recently, a simple semi-empiric calculation able to describe proton impact ionization for a wide variety of atomic and molecular targets was reported by Montenegro *et al.*²² Following Ref. 22, the ionization cross section by protons for an arbitrary target follows the simple scaling:

$$\frac{\sigma_{nl} I_{nl}^2}{Z_{nl} \delta_{nl}} = F \left(\frac{E/M}{I_{nl}} \right), \quad (1)$$

where

$$F(x) = \frac{A \ln(1 + Bx)}{x} - \frac{AB}{(1 + Cx)^4}, \quad (2)$$

with $A = 6.15 \times 10^3$, $B = 7.0 \times 10^{-2}$, $C = 1.4 \times 10^{-2}$, E/M in keV/amu, and the ionization potentials I_{nl} in atomic units for the cross section σ_{nl} in Mb. The label nl represents a particular atomic or molecular orbital.

For the electron case, we introduced here two changes in the above equations as an *ansatz* to take into account the sharp ionization threshold as well as the change in the shape of the cross section for energies below the maximum: $x = [1.836E \text{ (eV)}/I_{nl}] - 24.97$, and $C = 8.5 \times 10^{-3}$. Thus, at the threshold energy, $E \text{ (eV)} = 13.6 \times I_{nl} \text{ (a.u.)}$, $x = 0$ and $F(x) = 0$. These changes keep the coalescence of the electron and proton cross sections at high velocities.

The cross sections calculated as above, and shown in Figure 7(a), are the sum of the cross sections calculated for the pyrimidine molecular orbitals $7b_2$, $2b_1$, $11a_1$, $1a_2$, $10a_1$, $1b_1$, $6b_2$, $9a_1$, $5b_2$, $8a_1$, and $7a_1$, with ionization potentials 9.83, 10.4, 11.36, 11.28, 14.49, 14.49, 14.63, 16.25, 17.26, 18.25, and 20.6 eV, respectively.⁵⁰ For all orbitals $Z_{nl} = 2$, $\delta_{nl} = 0.66$, and all parameters but I_{nl} are the same. The parameter δ_{nl} synthesizes the particular details of each atomic or molecular orbital and was adjusted to give the better general agreement with the measured total ionization cross section. Inner orbitals contribute less than 5% of the total cross section. The calculated total ionization cross section (TCS), $\sum \sigma_{nl}$, summed for the molecular orbitals listed in Table II, is compared with the measured ones (summed cross section for all measured fragment ions) in Fig. 7(a). Below $v/v_0 \approx 3$, the calculated proton and electron total cross sections separate and, at our lower measured velocity, the calculated proton cross section is $\sim 13\%$ above the electron one. The agreement of these model calculations for both projectiles with the present measurements for the full measured energy range is remarkable.

In Figure 7(b), the absolute total non-dissociative ionization, the dissociative ionization, and the sum of both cross sections for proton and electron impact are displayed for equivalent velocities. The cross sections for the non-dissociative channel are the same for both projectiles due to our normalization procedure. In spite of that, the dissociative ones show a clear difference between protons and

TABLE II. Suggested fragmentation fractions, in percentage (1 = 100%), connecting the high-lying MOs of pyrimidine to the fragment ion produced through dissociative ionization. Measured (Exp. CS) and calculated (Cal. CS) cross sections for some (m/z) fragment ions, as well as the calculated ones for single ionization of each of the molecular orbitals (TCS), for 400 eV electrons, are included. All cross sections are in Mb units (10^{-18} cm²). The ionization potentials in eV (IP) of the 10 first molecular orbitals (MO) from Ref. 50 are also included.

		MO	7b2	2b1	11a1	1a2	10a1	1b1	6b2	9a1	5b2	8a1	SUM
		IP (eV)	9.83	10.4	11.36	11.28	14.49	14.49	14.63	16.25	17.26	18.26	
		TCS(Mb)	66.02	61.63	55.32	55.80	40.97	40.97	40.48	35.51	32.92	30.68	460.3
m/z	species	Exp. CS	Cal. CS	Percentage									
81	CC ₃ H ₄ N ₂	9.79	6.65	0.05	0.0435	0.006	0.006						6.65
80	C ₄ H ₄ N ₂	129.38	132.97	1	0.87	0.12	0.12						132.97
79	C ₄ H ₃ N ₂	6.10	6.15					0.075	0.075				6.15
54	C ₃ H ₄ N	4.74	4.16			0.027	0.027	0.013	0.015				4.16
53	C ₃ H ₃ N	82.37	83.15			0.54	0.54	0.26	0.305				83.15
52	C ₃ H ₂ N	37.01	37.78			0.34	0.34						37.78
51	C ₃ HN	19.48	20.48					0.25	0.25				20.48
50	C ₃ N	3.92	4.31		0.03			0.03	0.03				4.31
40	C ₂ H ₂ N	3.98	0.00										0.00
39	C ₂ HN	6.17	6.16		0.1								6.16
38	C ₃ H ₂	6.99	7.06									0.23	7.06
37	C ₃ H	3.16	3.29								0.1		3.29
28	HCNH	30.27	33.25				0.385	0.34		0.1			33.25
27	HCN	14.83	15.45						0.05	0.1	0.3		15.45
26	C ₂ H ₂	95.89	95.82						0.95	0.8	0.6	0.3	95.82
1	H	7.83	14.42									0.47	14.42

electrons. Indeed, although the dissociative cross section for both projectiles coalesces at high velocities, the proton dissociative cross section becomes approximately a factor of 1.6 larger than that for electrons at our lower measured velocity.

If the projectile velocity decreases and approaches the Bohr velocity of the inner molecular orbitals, the electron ionization cross section for these orbitals decreases sharply, while the proton cross section does not. Since the production of vacancies in the inner molecular orbitals results most certainly in molecular fragmentation, the dissociative cross sections by electron impact decrease when compared to the proton ones as the projectile velocity decreases, in accordance to our findings.

The total dissociative cross section is dominated by HCN and 2HCN losses ($m/z = 53$ and 26), which involves small energy transfers, as shown by the constancy of their ratios with respect to the parent ion for all measured velocities (see Figure 6). In such dynamical regime, it is expected that Born scaling is valid and electrons and protons have the same fragmentation cross sections, which is indeed the case. The possibility to observe differences between protons and electrons cross sections for molecular fragmentation, even in the Born regime, was raised by Wexler²⁰ years ago, and it is related to events with large momentum transfers, small cross sections and resulting in a strong molecular fragmentation. This might be the case of $m/z = 50$, where the proton cross sections are clearly above the electron ones for the whole range of measured velocities.

This is also the reason why the measured total ionization cross section for protons are larger than the calculated ones, at lower velocities, while for the electron case the agreement

seems to be better. The calculations consider just some of the outermost valence orbitals. While the innermost orbitals can hardly be accessed by low energy electrons, they can be accessed by low energy protons, and contribute significantly to the total fragmentation cross section.

F. Selected fragment ion cross section behavior as function of the velocity

In Figure 8, the fragment ions cross sections of the pathways associated to the simple and double loss of HCN, C₃H₃N⁺ + HCN and C₂H₂⁺ + 2HCN, respectively, are shown together with two other channels corresponding to three or more fragments: the break-up channel with the formation of

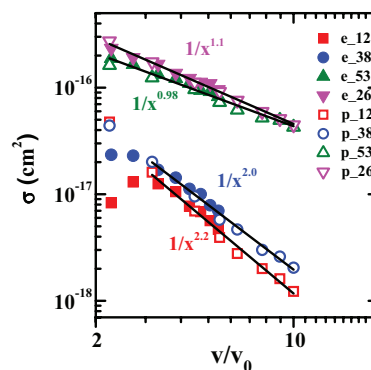


FIG. 8. Selected absolute partial dissociation cross section for both projectiles for different fragments belonging to the fragments groups A, B, C, and D. Functional curves describing a $1/(x)^n$ dependence, where $x = v/v_0$, for the fragments with $m/z = 12, 26, 38$, and 53 . Closed symbols are associated to electron impact; open symbols are related to proton collision.

C_3H_2^+ fragment and of the atomic C^+ ion. The figure includes cross sections for electron as well as for proton impact.

Above $3.5 v_0$, the cross sections for the fragments with $m/z = 26$ and 53 can be approximately described by a $1/x^n$ function, with $n \approx 1$, while the cross sections for the fragments with $m/z = 12$ and 38 are adjusted with $n \approx 2$. This clear functional difference in the velocity dependence of the cross sections suggests that single step ionization plays an important role for the former fragment production, while the latter involves two-step ionization with more extensive fragmentation.

IV. MODEL CALCULATION OF THE PARTIAL FRAGMENTATION CROSS SECTIONS: MOLECULAR ORBITAL ANALYSIS

Following the same line of reasoning described by Sigaud *et al.*²¹ in their study of CHClF_2 fragmentation by electron impact, we have chosen to describe the fragment formation through a scheme which matches the cross sections for the vacancy production in the various molecular orbitals, as given by Eq. (1), to the measured fragment ion cross sections, for both electron and proton impact. The main assumption of the model is that the fragmentation pattern is directly associated to—and it is a signature of—the molecular orbital where the primary vacancy is produced. This assumption is expected to be valid for swift projectiles, for which the collision time is much shorter than the fragmentation time.

The assignment of the fragmentation factors to each molecular orbital can be done using some guidance from a discussion about their appearance energies. Experimentally, the appearance energies were first reported in electron beam ionization experiments¹³ for only the 5 principal fragments, namely, the parent ion, the de-hydrogenated ion and the ionic fragments with $m/z = 26$, 52 , and 53 at energies of 9.83 , 13.01 , 15.79 , 15.01 , and 12.87 eV, respectively. Recently, also by means of electron impact (EI) experiments,¹² the appearance energies of 18 different ionic fragments were measured, their values ranging from 9.45 up to 21.6 eV. Applying the electron momentum spectroscopy (EMS) and the electron-electron coincidence (e, 2e) technique, the valence binding energies were assigned to the MOs structure of the molecule in combination with theoretical momentum distributions.^{15,16} Additionally, the (e, 2e) measurement^{15,16} succeeded in the identification of the nature of some MOs, e.g., $7b_2$ is a $2p$ -type MO.

The valence binding energies have also been obtained from photoionization investigations (PI) using He I radiation and synchrotron radiation.^{50–58} While the values extracted from EI yields^{12,13} are mostly slightly higher than those obtained by the PI yields,¹⁴ the values obtained from PES⁴⁹ and EMS^{15,16} measurements agree for almost all orbitals. A small difference can be expected as the photoionization process is subjected to different selection rules at the ionization thresholds compared to that induced by charged particles. The experimental results were compared against several calculations, such as Hartree-Fock (HF), outer valence Green function (OVGF), third-order algebraic diagrammatic construction (ADC3), density functional theory (DFT-B3LYP), and

statistical average of orbital potential (SAOP), as listed in Table 1 of Ref. 15. We adopted for our model calculation the ionization potential computed using the OVGF approach,⁵⁰ since its values present much better agreement with the first 10 MOs measured using charged particles as ionizing agent. A comparison between the experimental fragment appearance energies and calculations of individual molecular orbitals provided us background to our MOs assignment and population method.

The parent ion is formed mostly by the ionization of the outermost $7b_2$ valence orbital. In accordance to PIMS measurements of Plekan *et al.*,⁴⁵ the ionization of the first MO does not lead to fragmentation. The photoionization studies performed at 21 eV⁴⁵ and at 285.4 eV,^{51,52} measuring photoelectrons at selected energies in the range of $9 - 12$ eV in coincidence with mass spectra, already predict that the parent ion is also produced by the ionization of the $2b_1$, $11a_1$, and $1a_2$ valence orbitals, which have appearance energies ranging from 9.5 to 11.7 eV. The first four MOs give rise to the first three bands (first 3-fold peak structure) in the binding energy spectra.^{15,16,45,51,52}

The de-hydrogenated parent ion $m/z = 79$ has associated appearance energies of 10.7 and 12.5 eV. The fragment ion formation of mass $m/z = 53$ was observed starting at the energy of 11.3 eV^{45,51,52} or 11.65 eV,¹² 2.4 eV above the adiabatic ionization, up to 14.5 eV, as indicated on the high-binding side of the third peak (first structure) and the second peak structure, whereas a faint contribution can still be visible until 15.5 eV. The ionization of the MOs $11a_1$, $1a_2$, $10a_1$, and $1b_1$, related to this structure, is responsible for its production. The lower mass with $m/z = 52$ appears with a low yield from around 15.2 until 18 eV.^{51,52} The mass $m/z = 26$ has its dominant production occurring at around 15.7 eV (in the range of 15 up to 18 eV), but have the onset at around $14.2 - 14.5$ eV^{12,45,50,51} implying its origin from the higher MOs $10a_1$, $1b_1$, $6b_2$, $9a_1$, and $5b_2$. According to Bolognesi *et al.*,⁵¹ the mass $m/z = 28$ starts being produced at around 14.5 up to 18 eV, although Linert *et al.*¹² measured its appearance energy at 13.8 eV. The MOs associated to its formation would be $10b_1$, $1b_1$, $6b_2$, $9a_1$, $5b_2$, and $8a_1$. No other studies succeeded in the assignment of MOs to other ionic fragments.

Assuming a post-collisional fragmentation, a vacancy produced in a MO nl has a probability $f_{m,nl}$ to give rise to a recoil (fragment) ion with mass m . If σ_{nl} is the cross section for a vacancy production in the MO nl , the cross section σ_m to produce a fragment with mass m is given by

$$\sigma_m = \sum_{nl} f_{m,nl} \sigma_{nl}, \quad (3)$$

with

$$\sum_{nl} f_{m,nl} = 1. \quad (4)$$

Knowing σ_{nl} from Eq. (1), Eqs. (3) and (4) can be used to infer the fractions $f_{m,nl}$. Table II shows the suggested fragmentation fractions, in percentage ($1 = 100\%$), connecting the high-lying MOs of pyrimidine to the fragment ion produced

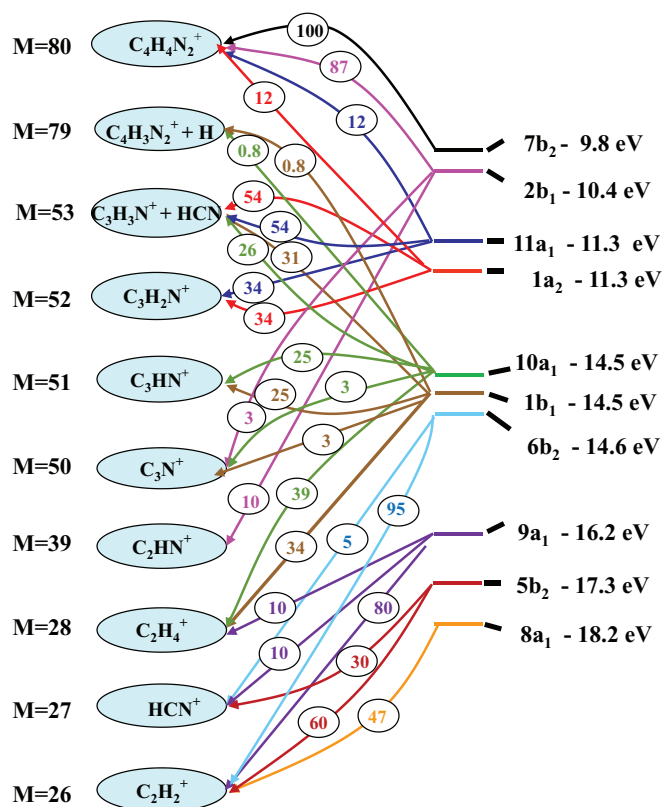


FIG. 9. Scheme of the suggested decay routes and branching ratios given in percentage for the dissociation of the pyrimidine molecule.

through dissociative ionization. The assignment of the fractions was carried out considering the discussion above about appearance energies, the constraint given by Eq. (4) (sum of fractions in each column is unity) and approximately matching the calculated to the measured cross section using Eq. (3). Naturally, the assignment is not unique and some freedom to change the tabulated values exists. However, the general picture of the fragmentation pattern cannot be much different due to the restrictions mentioned above associated to the determination of the fragment ion cross sections and the appearance energies. As a figure of merit, a change of 10% – 15% in the tabulated fractions clearly worsens the general agreement.

Figure 9 depicts the contribution of each MO for the formation of 9 fragments appearing in Table II. The cross sections of the first 10 MOs are distributed among the 14 fragments. These fractions can be used with the aid of Eqs. (1)–(3) to calculate the cross sections for the fragment ions and compare them with the measured ones, as a function of the projectile energy. This is shown in Figs. 10(a) and 10(b) for electron and proton impact, respectively. The same set of fragmentation fractions given in Table II is used for both projectiles.

The agreement is in general quite good for both projectiles. It should be remarked that the calculated fractions are not independent from one another but are linked through the scheme shown in Fig. 9, which gives support to the methodology used. However, it is noteworthy that the fragments with small cross sections, like those for masses $m/z = 50$, 27, and

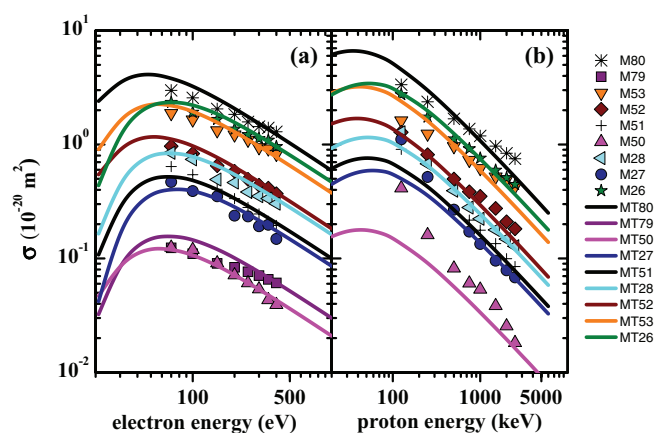


FIG. 10. Selected absolute partial dissociation cross sections (PDCS), where symbols designate the experimental cross sections and lines indicate the model calculated cross sections. (a) Electron impact PDCS for the 9 major fragments; (b) proton collision PDCS for 8 major fragments. The letter M designates the experimental cross sections while MT the model calculated values for the mass M .

51, present a marked difference between electron and proton impact, with the cross sections for the former being larger compared to the latter. It can be inferred that the production of these fragments involves large momentum transfers, favoring protons compared to electrons due to their greater mass, as indicated by Wexler,²⁰ and already mentioned at the end of Sec. III E. It is also clear that these differences tend to be smaller at high velocities, when the momentum transfer is small compared to the momentum of the impinging electron.

V. CONCLUSIONS

The measurement of the electron ionization and fragmentation cross sections and of the proton induced pure ionization and fragmentation yields at equivalent velocities, and in the range of validity of the Born approximation, allowed us to obtain and compare absolute total and partial cross sections for both charged projectiles. The normalization procedure used proved to be reliable and useful for showing where agreements or disagreements occur when comparing the fragmentation induced by the two projectiles.

At high velocities, the very good agreement between the observed yields for the more likely fragments produced by electron and proton impact corroborates our procedure. It is also shown that when the electron velocity decreases, approaching the maximum of the ionization cross section, the proton ionization cross section becomes larger than that for electrons. Thus, normalizing the cross sections for one projectile to the other is expected to be correct only if $(v/v_0) \geq 3$.

Fragment yields for the two projectiles are the same for most of the recoil ions, but protons are more efficient than electrons for those which have small cross sections and involve large momentum transfers. Most of the fragments are produced through a single step process, but from

the energy dependence of the cross section it is possible to identify those, such as $C_3H_2^+$, which are produced in two-step processes.

In addition to the parent molecular ion, the largest cross sections observed are those that result in one or two fragments of neutral HCN, corresponding to recoil ions with $m/z = 53$ or 26, respectively. According to the proposed fragmentation scheme, these fragments are induced by primary vacancies produced in the $11a_1$ and $1a_2$ MOs, in the former case, and in the inner $6a_2$, $9a_1$, and $5b_2$ MOs, in the latter case. To the authors' knowledge, this is the first time where such correlation is proposed in quantitative grounds.

This work shows that significant information about molecular fragmentation can be extracted from the measurement of absolute total and partial cross sections by electron and proton impact. The good agreement between experiment and present calculations strongly supports the use of this model and methodology as input in MOs assignments for other molecules and possibly, further on, in charged particle track structure modeling. Also, considering that the collision time of 400 eV electrons is of the order of a few attoseconds, the assumption that molecular fragmentation is a post-collisional process is fairly justified and the proposed

fragmentation yields should hold for photon induced vacancy production as well.

ACKNOWLEDGMENTS

The authors would like to acknowledge the following Brazilian agencies for the funding which made this work possible: Conselho Nacional de Desenvolvimento Científico e Tecnológico (CNPq), Coordenação de Aperfeiçoamento de Pessoal de Nível Superior (CAPES), Fundação de Amparo à Pesquisa do Estado do Rio de Janeiro (FAPERJ), and Ministério da Ciência e Tecnologia—Programa de Apoio à Núcleos de Excelência (MCT-Pronex).

APPENDIX: ABSOLUTE NON-DISSOCIATIVE AND PARTIAL DISSOCIATIVE CROSS SECTIONS

The numerical values of the absolute non-dissociative and partial dissociative cross sections for electron and proton impact on pyrimidine shown in Figures 3 and 5 are given in Tables III and IV, respectively.

TABLE III. Absolute non-dissociative and partial dissociative cross sections for the ejection of 25 positively charged fragments by electron impact at energies from 70 eV to 400 eV. The cross sections are in cm^2 , and the uncertainties are estimated below 6%.

m/z (a.u.)	Electron energy (eV)							
	70	100	150	200	250	300	350	400
1	1.85×10^{-17}	2.18×10^{-17}	1.87×10^{-17}	1.58×10^{-17}	1.20×10^{-17}	1.10×10^{-17}	9.58×10^{-18}	7.83×10^{-18}
12	8.31×10^{-18}	1.30×10^{-17}	1.25×10^{-17}	1.06×10^{-17}	7.74×10^{-18}	6.86×10^{-18}	5.65×10^{-18}	4.69×10^{-18}
13	8.48×10^{-18}	1.08×10^{-17}	8.30×10^{-18}	7.45×10^{-18}	5.68×10^{-18}	4.87×10^{-18}	3.92×10^{-18}	3.30×10^{-18}
14	2.41×10^{-18}	3.36×10^{-18}	3.68×10^{-18}	3.11×10^{-18}	2.45×10^{-18}	2.18×10^{-18}	1.62×10^{-18}	1.47×10^{-18}
15	7.55×10^{-19}	8.88×10^{-19}	6.88×10^{-19}	5.86×10^{-19}	5.13×10^{-19}	4.57×10^{-19}	3.83×10^{-19}	2.75×10^{-19}
24	6.04×10^{-18}	6.02×10^{-18}	5.45×10^{-18}	4.07×10^{-18}	3.14×10^{-18}	2.86×10^{-18}	2.45×10^{-18}	1.98×10^{-18}
25	2.59×10^{-17}	2.17×10^{-17}	1.78×10^{-17}	1.35×10^{-17}	1.11×10^{-17}	9.91×10^{-18}	8.82×10^{-18}	7.64×10^{-18}
26	2.34×10^{-16}	1.92×10^{-16}	1.66×10^{-16}	1.37×10^{-16}	1.22×10^{-16}	1.13×10^{-16}	1.09×10^{-16}	9.59×10^{-17}
27	4.69×10^{-17}	3.90×10^{-17}	3.51×10^{-17}	2.38×10^{-17}	2.34×10^{-17}	1.92×10^{-17}	1.98×10^{-17}	1.48×10^{-17}
28	8.46×10^{-17}	3.87×10^{-18}	2.98×10^{-18}	2.49×10^{-18}	2.55×10^{-18}	1.93×10^{-18}	2.31×10^{-18}	1.78×10^{-18}
29	4.59×10^{-18}	3.87×10^{-18}	2.98×10^{-18}	2.49×10^{-18}	2.55×10^{-18}	1.93×10^{-18}	2.31×10^{-18}	1.78×10^{-18}
36	2.99×10^{-18}	3.60×10^{-18}	2.87×10^{-18}	2.21×10^{-18}	1.67×10^{-18}	1.52×10^{-18}	1.18×10^{-18}	9.87×10^{-19}
37	1.13×10^{-17}	1.06×10^{-17}	7.73×10^{-18}	6.16×10^{-18}	5.11×10^{-18}	4.36×10^{-18}	3.48×10^{-18}	3.16×10^{-18}
38	2.35×10^{-17}	2.30×10^{-17}	1.69×10^{-17}	1.43×10^{-17}	1.12×10^{-17}	1.00×10^{-17}	7.89×10^{-18}	6.99×10^{-18}
39	2.08×10^{-17}	1.93×10^{-17}	1.47×10^{-17}	1.20×10^{-17}	1.02×10^{-17}	9.00×10^{-18}	7.34×10^{-18}	6.17×10^{-18}
40	1.29×10^{-17}	1.14×10^{-17}	8.69×10^{-18}	7.45×10^{-18}	6.22×10^{-18}	5.31×10^{-18}	4.53×10^{-18}	3.98×10^{-18}
41	2.39×10^{-18}	2.31×10^{-18}	1.88×10^{-18}	1.58×10^{-18}	1.18×10^{-18}	1.12×10^{-18}	9.40×10^{-19}	8.52×10^{-19}
50	1.25×10^{-17}	1.19×10^{-17}	9.10×10^{-18}	7.15×10^{-18}	6.09×10^{-18}	5.38×10^{-18}	4.33×10^{-18}	3.92×10^{-18}
51	6.41×10^{-17}	5.43×10^{-17}	4.05×10^{-17}	3.35×10^{-17}	2.80×10^{-17}	2.46×10^{-17}	2.12×10^{-17}	1.95×10^{-17}
52	9.66×10^{-17}	8.32×10^{-17}	6.52×10^{-17}	5.82×10^{-17}	4.95×10^{-17}	4.39×10^{-17}	4.14×10^{-17}	3.70×10^{-17}
53	1.88×10^{-16}	1.65×10^{-16}	1.33×10^{-16}	1.22×10^{-16}	1.10×10^{-16}	9.42×10^{-17}	9.19×10^{-17}	8.24×10^{-17}
54	1.02×10^{-17}	9.97×10^{-18}	7.96×10^{-18}	7.29×10^{-18}	6.79×10^{-18}	5.98×10^{-18}	5.51×10^{-18}	4.74×10^{-18}
79	1.24×10^{-17}	1.10×10^{-17}	9.04×10^{-18}	8.36×10^{-18}	7.64×10^{-18}	7.08×10^{-18}	6.55×10^{-18}	6.10×10^{-18}
80	2.99×10^{-16}	2.57×10^{-16}	2.05×10^{-16}	1.84×10^{-16}	1.58×10^{-16}	1.44×10^{-16}	1.40×10^{-16}	1.29×10^{-16}
81	2.40×10^{-17}	2.13×10^{-17}	1.48×10^{-17}	1.40×10^{-17}	1.20×10^{-17}	1.22×10^{-17}	1.01×10^{-17}	9.79×10^{-18}

TABLE IV. Absolute non-dissociative and partial dissociative cross sections for the ejection of 25 positively charged fragments for proton collision at energies from 125 keV to 2500 keV. The cross sections are in cm², and the overall uncertainty in the absolute cross-section values is below 10% and is marginally higher for fragments ions with low cross section values.

m/z (a.u.)	Proton energy (keV)							
	125	250	500	750	1000	1500	2000	2500
1	1.46×10^{-16}	5.97×10^{-17}	2.38×10^{-17}	1.46×10^{-17}	1.10×10^{-17}	7.37×10^{-18}	6.27×10^{-18}	5.07×10^{-18}
12	4.76×10^{-17}	1.61×10^{-17}	6.95×10^{-18}	3.93×10^{-18}	2.78×10^{-18}	2.01×10^{-18}	1.61×10^{-18}	1.23×10^{-18}
13	3.65×10^{-17}	1.52×10^{-17}	6.27×10^{-18}	3.50×10^{-18}	2.53×10^{-18}	1.82×10^{-18}	1.44×10^{-18}	1.18×10^{-18}
14	1.92×10^{-17}	7.16×10^{-18}	3.00×10^{-18}	1.79×10^{-18}	1.34×10^{-18}	9.57×10^{-19}	8.18×10^{-19}	5.76×10^{-19}
15	3.84×10^{-18}	1.45×10^{-18}	7.88×10^{-19}	3.29×10^{-19}	3.02×10^{-19}	2.18×10^{-19}	2.21×10^{-19}	1.23×10^{-19}
24	1.66×10^{-17}	6.58×10^{-18}	2.65×10^{-18}	1.54×10^{-18}	1.26×10^{-18}	7.97×10^{-19}	6.63×10^{-19}	4.86×10^{-19}
25	4.33×10^{-17}	2.16×10^{-17}	1.04×10^{-17}	7.43×10^{-18}	6.16×10^{-18}	4.13×10^{-18}	2.99×10^{-18}	2.47×10^{-18}
26	2.74×10^{-16}	1.74×10^{-16}	1.12×10^{-16}	9.18×10^{-17}	7.59×10^{-17}	5.95×10^{-17}	5.10×10^{-17}	4.46×10^{-17}
27	1.11×10^{-16}	5.19×10^{-17}	2.68×10^{-17}	1.72×10^{-17}	1.34×10^{-17}	9.56×10^{-18}	7.87×10^{-18}	6.82×10^{-18}
28	1.28×10^{-16}	6.77×10^{-17}	3.93×10^{-17}	2.80×10^{-17}	2.23×10^{-17}	1.78×10^{-17}	1.48×10^{-17}	1.28×10^{-17}
29	5.92×10^{-18}	4.00×10^{-18}	2.12×10^{-18}	1.53×10^{-18}	1.12×10^{-18}	8.84×10^{-19}	8.03×10^{-19}	6.47×10^{-19}
36	8.90×10^{-18}	3.11×10^{-18}	1.25×10^{-18}	8.40×10^{-19}	5.34×10^{-19}	3.47×10^{-19}	2.58×10^{-19}	1.75×10^{-19}
37	1.70×10^{-17}	8.27×10^{-18}	3.83×10^{-18}	2.64×10^{-18}	1.72×10^{-18}	1.28×10^{-18}	1.05×10^{-18}	7.69×10^{-19}
38	4.41×10^{-17}	2.01×10^{-17}	9.55×10^{-18}	5.77×10^{-18}	4.67×10^{-18}	3.00×10^{-18}	2.60×10^{-18}	2.05×10^{-18}
39	4.70×10^{-17}	1.93×10^{-17}	8.89×10^{-18}	5.78×10^{-18}	4.29×10^{-18}	3.40×10^{-18}	2.95×10^{-18}	2.11×10^{-18}
40	2.32×10^{-17}	1.13×10^{-17}	6.07×10^{-18}	3.78×10^{-18}	2.62×10^{-18}	1.96×10^{-18}	1.65×10^{-18}	1.37×10^{-18}
41	1.54×10^{-18}	1.33×10^{-18}	1.23×10^{-18}	7.71×10^{-19}	4.69×10^{-19}	2.76×10^{-19}	2.65×10^{-19}	2.03×10^{-19}
50	4.14×10^{-17}	1.61×10^{-17}	8.20×10^{-18}	6.06×10^{-18}	5.35×10^{-18}	3.84×10^{-18}	2.55×10^{-18}	1.82×10^{-18}
51	9.07×10^{-17}	5.25×10^{-17}	2.70×10^{-17}	2.17×10^{-17}	1.77×10^{-17}	1.35×10^{-17}	9.95×10^{-18}	8.49×10^{-18}
52	1.28×10^{-16}	8.14×10^{-17}	4.98×10^{-17}	3.85×10^{-17}	3.51×10^{-17}	2.75×10^{-17}	2.10×10^{-17}	1.82×10^{-17}
53	1.62×10^{-16}	1.24×10^{-16}	9.62×10^{-17}	7.29×10^{-17}	6.18×10^{-17}	5.21×10^{-17}	4.95×10^{-17}	4.27×10^{-17}
54	5.76×10^{-18}	5.28×10^{-18}	5.11×10^{-18}	3.59×10^{-18}	2.79×10^{-18}	2.30×10^{-18}	2.25×10^{-18}	2.10×10^{-18}
79 + 80 + 81	3.35×10^{-16}	2.37×10^{-16}	1.68×10^{-16}	1.37×10^{-16}	1.19×10^{-16}	9.68×10^{-17}	8.38×10^{-17}	7.50×10^{-17}

- ¹G. Garcia, G. Tejedor, and M. C. Fuss, *Radiation Damage in Biomolecular Systems*, Biological and Medical Physics, Biomedical Engineering (Springer, Germany, 2012), and references therein.
- ²J. M. Rice, G. O. Dudek, and M. Barber, *J. Am. Chem. Soc.* **87**(20), 4569–4576 (1965).
- ³P. G. Stoks and A. W. Schwartz, *Geochim. Cosmochim. Acta* **45**(4), 563–569 (1981).
- ⁴O. Botta and J. L. Bada, *Surv. Geophys.* **23**(5), 411–467 (2002).
- ⁵S. B. Charnley, Y.-J. Kuan, H.-C. Huang, O. Botta, H. M. Butner, N. Cox, D. Despois, P. Ehrenfreund, Z. Kisiel, Y.-Y. Lee, A. J. Markwick, Z. Peeters, and S. D. Rodgers, *Adv. Space Res.* **36**(2), 137–145 (2005).
- ⁶Y.-J. Kuan, C.-H. Yan, S. B. Charnley, Z. Kisiel, P. Ehrenfreund, and H.-C. Huang, *Mon. Not. R. Astron. Soc.* **345**(2), 650–656 (2003).
- ⁷M. Nuevo, S. N. Milam, S. A. Sandford, J. E. Elsila, and J. P. Dworkin, *Astrobiology* **9**(7), 683–695 (2009).
- ⁸P. P. Bera, M. Nuevo, S. N. Milam, S. A. Sandford, and T. J. Lee, *J. Chem. Phys.* **133**(10), 104303-1–104303-7 (2010).
- ⁹K. Biemann and J. A. McCloskey, *J. Am. Chem. Soc.* **84**(10), 2005–2007 (1962).
- ¹⁰J. M. Rice and G. O. Dudek, *J. Am. Chem. Soc.* **89**(11), 2719–2725 (1967).
- ¹¹G. Milani-Nejad and H. D. Stidham, *Spectrochim. Acta* **31A**, 1433–1453 (1975).
- ¹²I. Linert, M. Dampc, B. Mielewska, and M. Zubek, *Eur. Phys. J. D* **66**(1), 20 (2012).
- ¹³J. Momigny, J. Urban, and H. Wankenne, *Bull. Soc. R. Sci. Liège* **34**, 337–340 (1965).
- ¹⁴M. Schwell, H.-W. Jochims, H. Baumgärtel, and S. Leach, *Chem. Phys.* **353**(1-3), 145–162 (2008).
- ¹⁵C. G. Ning, K. Liu, Z. H. Luo, S. F. Zhang, and J. K. Deng, *Chem. Phys. Lett.* **476**(4-6), 157–162 (2009).
- ¹⁶J. D. Builth-Williams, S. M. Bellm, D. B. Jones, H. Chaluvadi, D. H. Madison, C. G. Ning, B. Lohmann, and M. J. Brunger, *J. Chem. Phys.* **136**(2), 024304-1–024304-6 (2012).
- ¹⁷J. D. Hein, H. Al-Khazraji, C. J. Tiessen, D. Lukic, J. A. Trocchi, and J. W. McConkey, *J. Phys. B: At. Mol. Opt. Phys.* **46**(4), 045202-1–045202-4 (2013).
- ¹⁸L. D. Fondren, J. McLain, D. M. Jackson, N. G. Adams, and L. M. Babcock, *Int. J. Mass Spectrom.* **265**(1), 60–67 (2007).
- ¹⁹E. Mendoza, G. C. Almeida, D. P. P. Andrade, H. Luna, W. Wolff, M. L. M. Rocco, and H. M. Boechat-Roberty, *Mon. Not. R. Astron. Soc.* **433**(4), 3440–3452 (2013).
- ²⁰S. Wexler, *J. Chem. Phys.* **41**(9), 2781–2790 (1964).
- ²¹L. Sigaud, N. Ferreira, V. L. B. de Jesus, W. Wolff, A. L. F. de Barros, A. C. F. dos Santos, R. S. Menezes, A. B. Rocha, M. B. Shah, and E. C. Montenegro, *J. Phys. B: At. Mol. Opt. Phys.* **43**(10), 105203-1–105203-9 (2010).
- ²²E. C. Montenegro, G. M. Sigaud, and R. D. Dubois, *Phys. Rev. A* **87**(1), 012706-1–012706-15 (2013).
- ²³W. Wolff, I. J. de Souza, A. C. Tavares, G. F. S. de Oliveira, and H. Luna, *Rev. Sci. Instrum.* **83**, 123107-1–123107-8 (2012).
- ²⁴J. S. Ihani, H. Luna, W. Wolff, and E. C. Montenegro, *J. Phys. B: At. Mol. Opt. Phys.* **46**(11), 115208-1–115208-9 (2013).
- ²⁵N. Ferreira, L. Sigaud, V. L. B. de Jesus, A. B. Rocha, L. H. Coutinho, and E. C. Montenegro, *Phys. Rev. A* **86**, 012702-1–012702-5 (2012).
- ²⁶N. Takahashi, S. Hosokawa, M. Saito, and Y. Haruyama, *Phys. Scr.* **T144**, 014057-1–014057-3 (2011).
- ²⁷J. Jones, G. B. Bacskey, J. C. Mackie, and A. Doughty, *J. Chem. Soc. Faraday Trans.* **91**(11), 1587–1592 (1995).
- ²⁸D. Lipkind and J. S. Chickos, *Struct. Chem.* **20**(1), 49–58 (2009).
- ²⁹P. Colarusso, K. Zhang, B. Guo, and P. F. Bernath, *Chem. Phys. Lett.* **269**(1-2), 39–48 (1997).
- ³⁰J. de Vries, R. Hoekstra, R. Morgenstern, and T. Schlathöler, *J. Phys. B: At. Mol. Opt. Phys.* **35**(21), 4373–4381 (2002).
- ³¹S. Feil, K. Gluch, S. Matt-Leubner, P. Scheier, J. Limtrakul, M. Probst, H. Deutsch, K. Becker, A. Stamatovic, and T. D. Märk, *J. Phys. B: At. Mol. Opt. Phys.* **37**(15), 3013–3020 (2004).
- ³²B. Coupier, B. Farizon, M. Farizon, M. J. Gaillard, F. Gobet, N. V. de Castro Faria, G. Jalbert, S. Ouaskit, M. Carré, B. Gstyr, G. Hanel, S. Deniff, L. Feketeova, P. Scheier, and T. D. Märk, *Eur. Phys. J. D* **20**(3), 459–468 (2002).
- ³³F. Alvarado, S. Bari, R. Hoekstra, and T. Schlathöler, *J. Chem. Phys.* **127**(3), 034301-1–034301-7 (2007).

- ³⁴A. Le Padellec, P. Moretto-Capelle, M. Richard_Viard, J. P. Champeaux, and P. Cafarelli, *J. Phys.: Conf. Ser.* **101**, 012007-1–012007-6 (2008).
- ³⁵J. Tabet, S. Eden, S. Feil, H. Abdoul-Carime, B. Farizon, M. Farizon, S. Ouaskit, and T. D. Märk, *Int. J. Mass Spectrom.* **292**(1–3), 53–63 (2010).
- ³⁶J. Tabet, S. Eden, S. Feil, H. Abdoul-Carime, B. Farizon, M. Farizon, S. Ouaskit, and T. D. Märk, *Phys. Rev. A* **82**(2), 022703-1–022703-5 (2010).
- ³⁷G. Vall-Illósera, M. Coreno, P. Erman, M. A. Huels, K. Jakubowska, A. Kivimäki, E. Rachlew, and M. Stankiewicz, *Int. J. Mass Spectrom.* **275**(1–3), 55–63 (2008).
- ³⁸M.-F. Lin, Y. A. Dyakov, C.-M. Tseng, A. M. Mebel, S. H. Lin, Y. T. Lee, and C.-K. Ni, *J. Chem. Phys.* **124**, 084303-1–084303-8 (2006).
- ³⁹H. C. Straub, P. Renault, B. G. Lindsay, K. A. Smith, and R. F. Stebbings, *Phys. Rev. A* **54**(3), 2146–2153 (1996).
- ⁴⁰R. Buff and J. Dannacher, *Int. J. Mass Spectrom. Ion Processes* **62**(1), 1–15 (1984).
- ⁴¹H.-W. Jochims, M. Schwell, J.-L. Chotin, M. Clemino, F. Dulieu, H. Baumgärtel, and S. Leach, *Chem. Phys.* **298**(1–3), 279–297 (2004).
- ⁴²H.-W. Jochims, M. Schwell, M. Baumgärtel, and S. Leach, *Chem. Phys.* **314**(1–3), 263–282 (2005).
- ⁴³A. F. Lago, L. H. Coutinho, R. R. T. Marinho, A. Naves de Brito, and G. G. B. de Souza, *Chem. Phys.* **307**(1), 9–14 (2004).
- ⁴⁴L. H. Coutinho, M. G. P. Homem, R. L. Cavasso-Filho, R. R. T. Marinho, A. F. Lago, G. G. B. de Souza, and A. Naves de Brito, *Br. J. Phys.* **35**(4A), 940–944 (2005).
- ⁴⁵O. Plekan, M. Coreno, V. Feiger, A. Moise, R. Richter, M. de Simone, R. Sankari, and K. C. Prince, *Phys. Scr.* **78**, 058105-1–058105-6 (2008).
- ⁴⁶W. Hwang, Y.-K. Kim, and M. E. Rudd, *J. Chem. Phys.* **104**, 2956–2966 (1996).
- ⁴⁷C. Champion, *J. Chem. Phys.* **138**, 184306-1–184306-8 (2013).
- ⁴⁸I. Shafranyosh, M. I. Sukhoviya, and M. I. Shafranyosh, *J. Phys. B: At. Mol. Opt. Phys.* **39**, 4155–4162 (2006).
- ⁴⁹C. Q. Jiao, C. A. DeJoseph, Jr., R. Lee, and A. Garscadden, *Intern. J. Mass Spectrom.* **257**, 34–40 (2006).
- ⁵⁰A. W. Potts, D. M. Holland, A. B. Trofimov, J. Schirmer, L. Karlsson, and K. Siegbahn, *J. Phys. B: At. Mol. Opt. Phys.* **36**(14), 3129–3143 (2003).
- ⁵¹P. Bolognesi, P. O’Keeffe, V. Feyer, O. Plekan, K. Prince, M. Coreno, G. Mattioli, A. A. Bonapasta, W. Zhang, V. Carravetta, Y. Ovcharenko, and L. Avaldi, *J. Phys.: Conf. Ser.* **212**, 012002-1–012002-6 (2010).
- ⁵²P. Bolognesi, M. C. Castrovilli, P. O’Keeffe, A. R. Casavola, D. Catone, S. Turchini, and L. Avaldi, *Nucl. Instrum. Methods Phys. Res., Sect. B* **279**, 118–123 (2012).
- ⁵³M. N. Piancastelli, P. R. Keller, J. W. Taylor, F. A. Grimm, and T. A. Carlson, *J. Am. Chem. Soc.* **105**(13), 4235–4239 (1983).
- ⁵⁴P. O’Keeffe, P. Bolognesi, A. R. Casavola, D. Catone, N. Zema, S. Turchini, and L. Avaldi, *Mol. Phys.* **107**, 2025–2037 (2009).
- ⁵⁵W. von Niessen, W. P. Kraemer, and G. H. F. Dierksen, *Chem. Phys.* **41**(1–2), 113–132 (1979).
- ⁵⁶R. Gleiter, E. Heilbronner, and V. Hornung, *Helv. Chim. Acta* **55**(1), 255–274 (1972).
- ⁵⁷M. J. S. Dewar and S. D. Worley, *J. Chem. Phys.* **51**(1), 26–267 (1969).
- ⁵⁸D. M. P. Holland, A. W. Potts, L. Karlsson, M. Stener, and P. Decleva, *Chem. Phys.* **390**(1), 25–35 (2011).